

Analysis of Interfacial Processes at the SOFC Electrodes By *in-situ* Raman Spectroscopy

D. A. Agarkov, I. N. Burmistrov, F. M. Tsybrov, I. I. Tartakovskii, V. V. Kharton,
S. I. Bredikhin and V. V. Kveder

Institute of Solid State Physics RAS, Chernogolovka, Moscow Distr. 142432, Russia

The present work is centered on the development of a new technique for *in-situ* Raman spectroscopy studies of local chemical and electrochemical reactions, phase transitions, strains and morphological alterations in the SOFC electrodes under working conditions, combined with electrochemical measurements. An appropriate selection of the electrodes geometry makes it possible to directly collect Raman spectra from the triple-phase boundary zone by passing the beam through transparent single-crystal solid electrolyte onto the interface, varying current density, temperature and atmosphere over the working electrode. The results of case studies, focused on reduction of Ni-containing cermet anodes, are presented.

Introduction

Kinetics of redox processes and the variations of charge-carrier concentrations across the SOFC electrode / electrolyte interfaces have a critical importance for the fuel cell performance. The microscopic reaction mechanisms in the vicinity of triple-phase boundary (TPB) can be assessed by the electrochemical methods, such as impedance spectroscopy, current-voltage measurements and various pulse techniques. Except for the micro-electrode approaches, however, these methods are cumulative. Moreover, unambiguous interpretation of the electrochemical measurement results requires, as a rule, use of complementary experimental techniques and/or simplified kinetic models. Important additional information essential for understanding of the electrode kinetics can be collected employing Raman spectroscopy. The latter is a non-destructive and non-invasive technique providing powerful tools for real-time SOFC characterization (1). Raman spectroscopy is widely used to characterize solid oxide electrolytes (*e.g.*, see (2-4)), anode materials (5-7), cathodes (8-10), glass sealants (11-13) and current collectors (14-16). Furthermore, present or potential applications of micro-Raman spectroscopy include *in-situ* analysis of fuel oxidation (17), sulfur poisoning (18), carbon formation (19-21) and dissolution (22), phase transitions (23), reactions involving gaseous species (24) and mechanical stresses (25). As an example, the combined studies (17) by *in-situ* Raman spectroscopy and current voltammetry made it possible to directly estimate the formation of graphitic intermediates in the course of CO and butane fuel oxidation in SOFCs. Another approach (21) correlating the vibrational Raman spectra with chronopotentiometry showed important relationships between carbon deposition and cell potential.

This work is centered on the developments of a new combined technique for *in-situ* Raman spectroscopy analysis of the electrochemical reaction zone at the electrode | solid

oxide electrolyte interface. For most approaches known in the literature (*e.g.*, (17-25)), the Raman spectra are mainly related to the outer boundaries of model electrochemical cells, primarily to the electrode surface, a result of low penetration depth of the excitation radiation. However, the performance-governing interfacial zones of the electrode systems, where change of carrier type takes place, cannot be achieved viewing the surface and edge areas. In the present work, this problem was solved by employing optically transparent, single-crystal membranes made of 10 mol.% Sc_2O_3 and 1% mol.% Y_2O_3 stabilized zirconia (10Sc1YSZ). In order to provide simultaneous Raman and electrochemical measurements of the model cell placed under SOFC operation conditions, a special controlled-atmosphere chamber was elaborated and tested. An appropriate selection of the electrodes geometry makes it possible to directly collect Raman spectra from the triple-phase (TPB) zone, passing the beam through single-crystal solid electrolyte onto the electrode | electrolyte interface polarized under given external conditions. The case studies using this approach were focused on the redox kinetics of standard Ni-containing cermet anodes.

Experimental

Electrochemical Cell Geometry

The developments of combined experimental setup described in this report were aimed at providing *in situ* Raman spectroscopy analysis of the interface between working electrode (WE) and solid electrolyte (SE) membrane, optically transparent in visible light, as a function of current density, atmosphere and temperature. The WE (anode in the present case) had a standard circular shape. The counter electrode (CE) should provide an optically transparent zone enabling the laser excitation to reach the WE | SE interface. In this work, a radially symmetric CE (Fig.1) was selected. In order to provide minimum local deviations in the current density distribution, the size of the central hole was chosen minimum enabling passing the laser beam. When necessary, the selected geometry makes it possible to introduce an additional reference electrode, which should be preferably located at the SE edge.

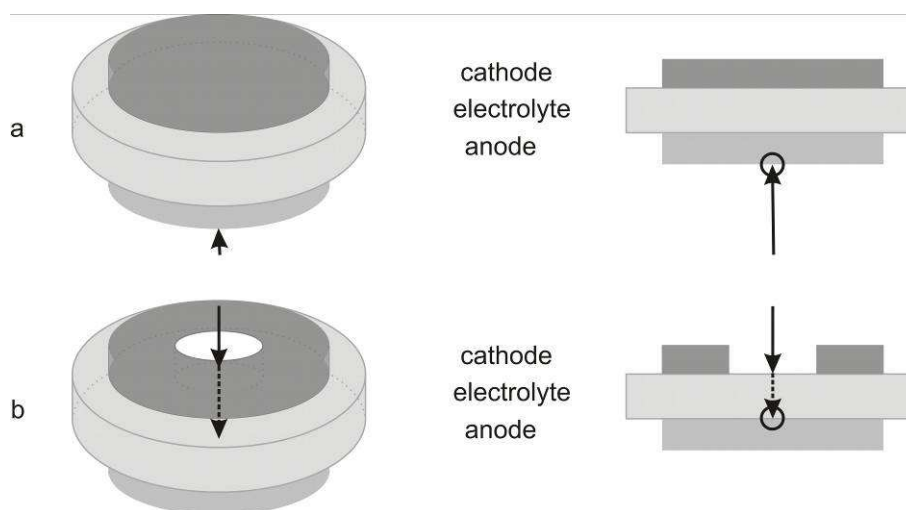


Figure 1. Electrochemical cell geometry: (a), standard SOFC; (b), electrode configuration for the studies of the solid electrolyte | anode interface tested in this work.

Single-Crystal Electrolyte Membranes

The transparent single crystals of cubic zirconia stabilized by 10 mol.% Sc_2O_3 and 1 mol.% Y_2O_3 (10Sc1YSZ) were grown employing direct melt crystallization technique in a cold crucible at the Institute of General Physics RAS (26,27). The electrical properties of these crystals were reported elsewhere (28). In particular, at 850°C the ionic conductivity of 10Sc1YSZ is higher than 0.12 S/cm (28), which ensures a high performance of planar solid electrolyte membranes. The crystals were cut by a diamond saw into discs (diameter of 21 mm), then thinned down to 250 and $500 \mu\text{m}$.

One single-crystal disk was used to estimate the effects of polishing. At each side of the disk, a half of the surface was polished; these half-circles were perpendicular to one another (inset in Fig.2) in order to provide 4 possible combinations of polished and unpolished surfaces. Then a layer of NiO-based composite was deposited onto the anode-side surface and sintered under standard conditions used for the anode fabrication, as described below. The Raman spectra of the anode | electrolyte interface (Fig.2) were collected in the 4 zones of this sample using the same regime of the optical system, at room temperature. For the membrane quarter with two unpolished surfaces, the characteristic peaks of NiO are invisible. A similar situation, namely poor resolution of the 2P peak ($\sim 1150 \text{ cm}^{-1}$), is observed when the anode size surface of the solid electrolyte crystal was only polished (Fig.2a). The characteristic bands (1150 cm^{-1} and 1460 cm^{-1}) can be clearly distinguished in the Raman spectra when either both surfaces or cathode-side surface were polished. At the same time, SEM analysis of the porous electrode layers deposited onto polished and unpolished zirconia surfaces, showed that latter provides a substantially better adhesion of the electrode. Consequently, only the cathode (CE) side surfaces of the single-crystal membranes were polished for the model cell fabrication.

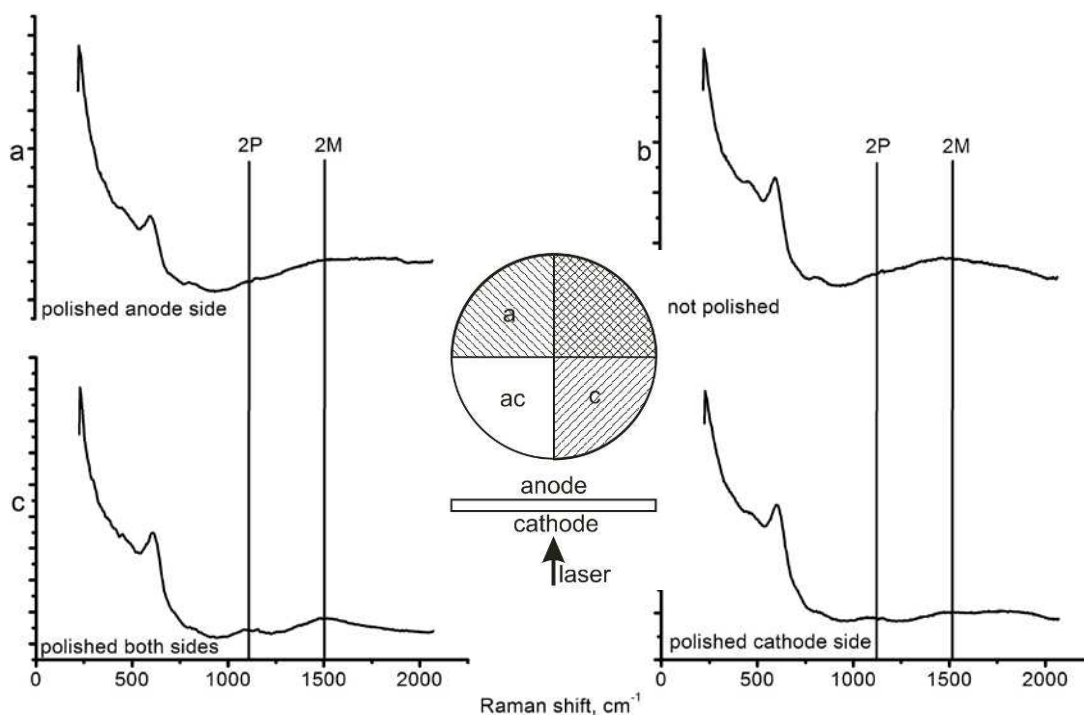


Figure 2. Comparison of the Raman spectra collected for 4 different combinations of the SE membrane polished surfaces: (a), polished anode-side surface; (b), two unpolished surfaces; (c), two polished surfaces; (d), polished cathode-side surface.

Electrode Deposition

Both anode and cathode of the model cells comprised two layers: functional and current-collecting. The electrode architecture and fabrication conditions, described below, were selected on the basis of previous results (30). The functional anode layer, which is directly deposited onto the SE membrane, was prepared from submicron NiO (Sigma Aldrich, USA) pre-annealed in air at 700°C for 2 h. A mixture of NiO (40 wt.%) and 10 mol.% Sc₂O₃ + 1 mol.% CeO₂ stabilized zirconia (10Sc1CeSZ, DKKK, Japan, 60 wt.%) was ball-milled for 1 h, followed by annealing at 500°C for 3 h.

The current-collecting layer of the anode, which should have a high electronic conductivity in combination with high porosity, was prepared from the same starting powders mixed in the weight ratio 60:40. An addition of pore-forming agent, 10 wt.% rice starch (Amidon Royal de Riz, Belgium) was also introduced in this mixture prior to ball-milling.

Submicron powder of (La_{0.8}Sr_{0.2})_{0.95}MnO₃ (LSM) used for the cathode was prepared via citrate synthesis route (29), with final annealing in air at 1100°C for 5 h. The functional cathode layer consisted of 60 wt.% LSM and 40 wt.% 10Sc1CeSZ. The current-collecting layer of the cathode was made of pure LSM.

All the powders were ball-milled in a mixture of toluene, butanol and diethyl adipate (69/29/2 vol.%) in the presence of 3 wt.% diaminopropane. In order to prepare pastes for screen-printing, the powders were mixed with Heraeus V-006A thinner (Germany) in a planetary mixer (Thinky, USA); the powder to thinner mass ratio was 1:0.5 for both anode pastes, 1:0.8 for the cathode functional layer and 1:1 for the cathode current-collecting layer. The pastes were deposited onto the single-crystal membrane using an Ekra Mat S-45 screen printer (Germany), with drying of each layer at 130°C. The anode was sintered in air at 1250°C for 3 h; its reduction was performed in the course of Raman measurements. The cathode layer was finally annealed in air at 1100°C for 4 h.

Characterization of Materials and Electrochemical Cells

All the electrode materials were examined by X-ray diffraction (XRD), thermogravimetric analysis (TGA), and scanning and transmission electron microscopy (SEM/TEM) coupled with energy-dispersive spectroscopic analysis (EDS). XRD and TGA studies were performed using Siemens D-500-Braun and Setaram Setsys EVO 16/18 instruments, respectively. SEM/EDS analyses were carried out using Supra 50-VP microscope (Oxford, UK). A Jeol JEM 100 CX-II instrument (Japan) was employed for TEM.

Results and Discussion

NiO Powder and Porous Layers

XRD showed that NiO used for the case studies is single-phase. No cation impurities were found by EDS within the detection limits. According to TGA and TEM analyses, however, the as-received NiO powder contained hyperstoichiometric oxygen

incorporated into the surface layers of nano-sized particles. Annealing at 700°C in air makes it possible to remove the absorbed oxygen and to moderately increase particle size, thus providing a good adhesion and microstructural stability of the sintered electrode layers. The electrode microstructures are illustrated by Fig.3. The thicknesses of anode functional and current-collecting layers were approximately 20 and 25 μm , respectively.

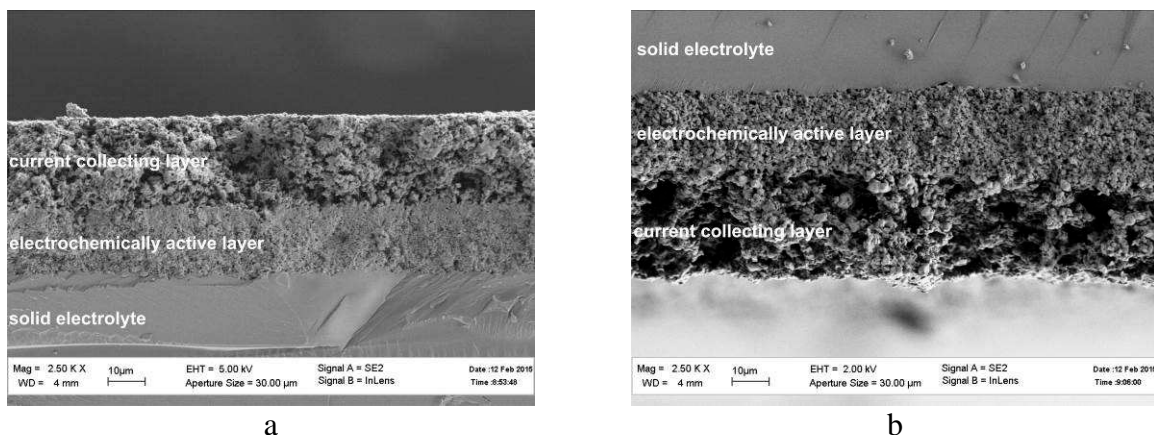


Figure 3. SEM micrographs of fractured electrochemical cell: (a) anode; (b) cathode side.

Controlled-Atmosphere Chamber and Optical System

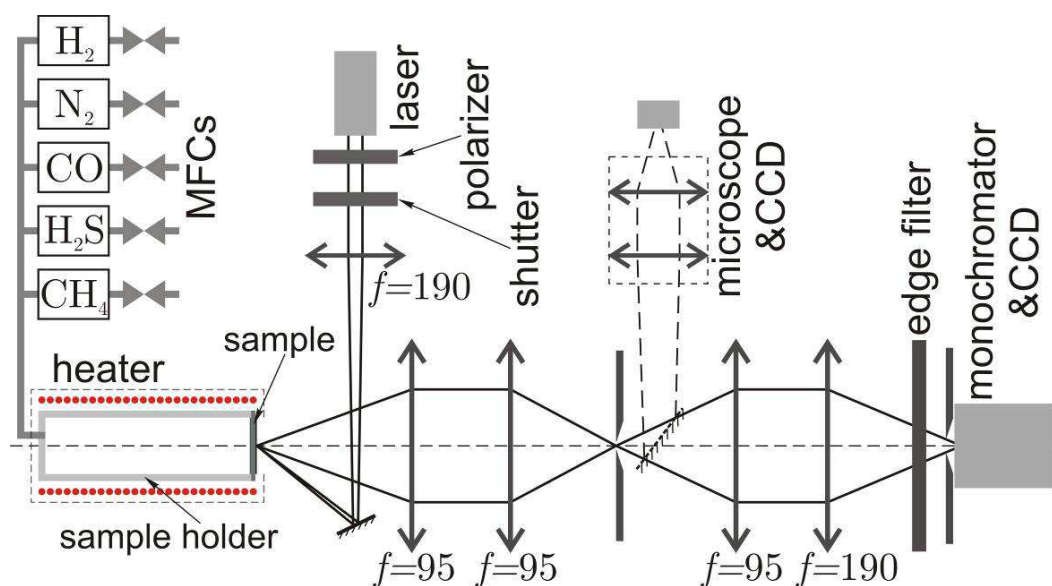


Figure 4. Schematic drawing of the experimental setup (see text).

Figure 4 presents a general scheme of the developed experimental setup, which comprises a gas-mixing system equipped with mass-flow controllers (MFC - Bronkhorst, Netherlands), high-temperature chamber with a transparent single-crystal zirconia membrane (Fig.1b), and an optical system for the Raman spectroscopy studies. Raman scattering in the working electrodes was excited by a 30 mW green (532 nm) laser. The system components include a polarizer decreasing power of the laser radiation when necessary, a shutter stopping the excitation beam for system tuning, and a collecting lens (focus distance of 190 mm) to focus the beam on a selected region of the interface or

electrode. The excitation beam is reflected by a mirror after the focusing lens, placed beside the optical axis in order to avoid specks and parasite reflections. The Raman scattering radiation is collected by a collecting lens with focus distance of 95 mm; the WE electrode is located in one of its focuses. Another lens with the same focus distance focuses radiation inside the crossed optical gaps, used to limit the visible region. One movable mirror after the gaps enables to direct the radiation to an optical microscope with 5.1 megapixel CCD camera. If the movable mirror is removed, the excited radiation can be collected by a second pair of collecting lenses with the focus distances of 95 and 190 mm. The scattered light was distributed into different angle directions by a diffraction grating monochromator MDR-12 (LOMO, Russia), and registered by a CCD camera (Princeton Instruments, USA) with 512x512 pixel resolution. All the lenses used for the setup were produced by the Lytkarino Optical Glass Factory (Russia).

The Raman spectra presented in this work were obtained as a sum of 100 spectra, collected for 2 seconds each; the background spectra obtained under identical conditions with the laser switched off were automatically subtracted.

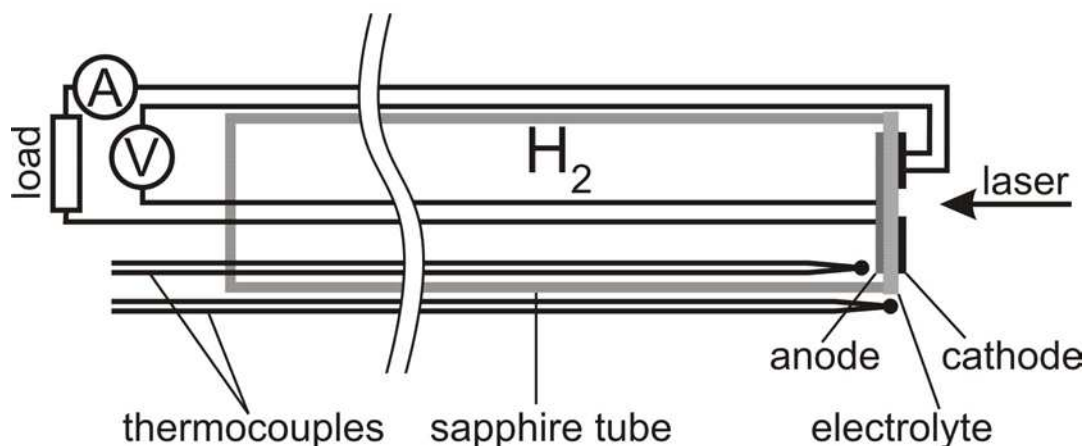


Figure 5. Schematic drawing of the high-temperature sample holder.

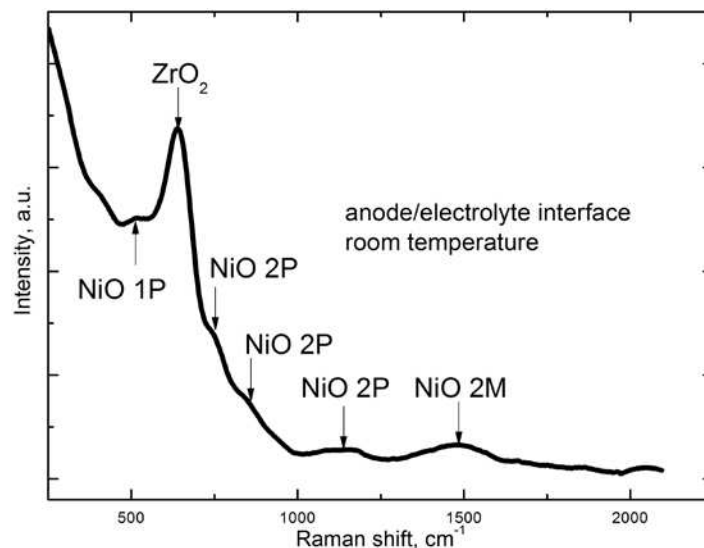


Figure 6. Room-temperature Raman spectrum of as-sintered anode | electrolyte interface prior to reduction.

The electrochemical cell holder inserted in the high-temperature furnace with a glass window (Fig.4) is schematically shown in Fig.5. The holder comprises a single-crystal sapphire tube (outer diameter of 21 mm), two thermocouples and Pt current collectors. The single-crystal zirconia membrane with electrodes (Fig.1b) is hermetically sealed onto one end of the sapphire tube. The atmosphere over the working electrode can be precisely controlled by the gas mixing system.

Validation of the Experimental Approach: NiO Reduction at the Interface

A typical Raman spectrum of the as-prepared anode | electrolyte interface is presented in Fig. 6. The peak at 515 cm^{-1} corresponds to 1P (1 phonon) oscillations in NiO; 740 , 860 and 1150 cm^{-1} – to 2P oscillations; the peak at 1460 cm^{-1} results from 2M (magnon) oscillations. The strongest peak at $\sim 640\text{ cm}^{-1}$ is characteristic of cubic zirconia in the composite electrode and solid-electrolyte membrane. The NiO peaks at 515 , 740 and 860 cm^{-1} cannot be used to detect phase transformations in the anode as these are located close to the strongest zirconia peak. The most indicative are the peaks at 1150 and 1460 cm^{-1} , having a good resolution at room temperature. However, the 2M (1460 cm^{-1}) peak becomes much weaker at 200°C and disappears at 252°C due to transformation of antiferromagnetic NiO to cubic beta-NiO (Fig.7). The phonon peak at 1150 cm^{-1} is, therefore, the only peak in the Raman spectrum which can be used to study NiO reduction or current-induced oxidation of metallic Ni at the interface. Notice also that the Raman spectrum collected at 600°C suffers from heat radiation, thus introducing additional experimental limitations.

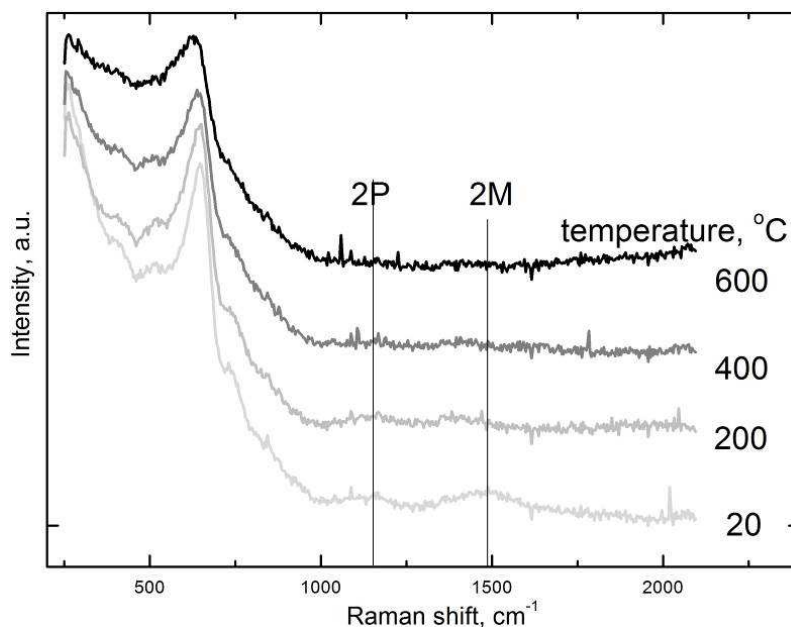


Figure 7. Raman spectra of NiO-10Sc1CeSZ composite anode on heating in air.

The NiO reduction tests in flowing H_2 were hence performed at 500°C . In the course of these experiments, the gas flow rate over the anode was fixed at 100 ml/min ; the Raman spectra were collected each 200 seconds. As expected, the reduction leads to monotonic changes in the spectra (Fig.8), primarily in the vicinity of 1150 cm^{-1} peak.

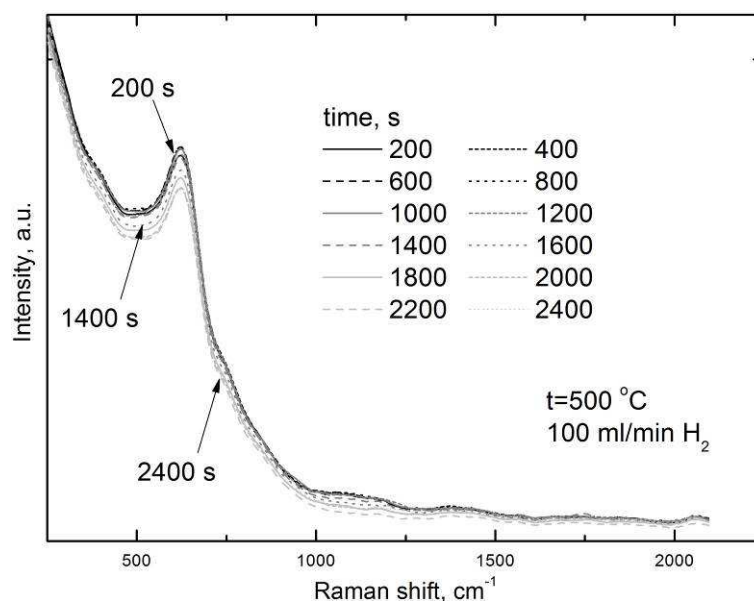


Figure 8. Raman spectra of the composite anode on reduction in hydrogen.

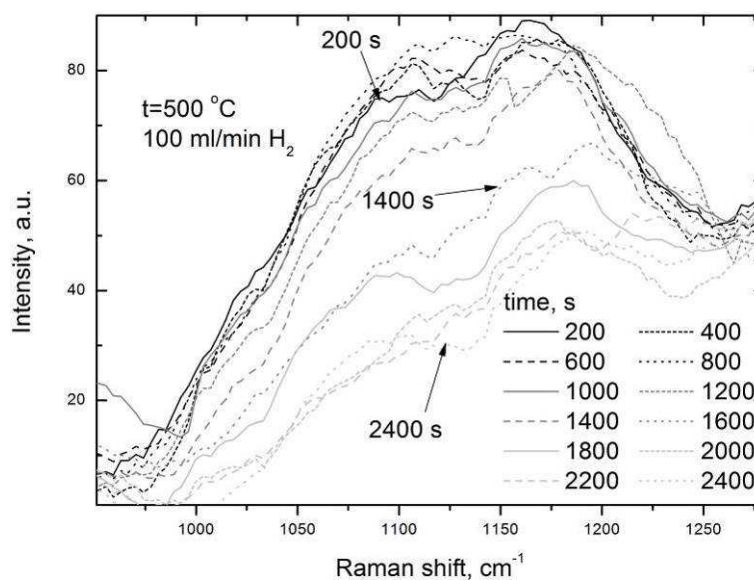


Figure 9. Characteristic fragments of the composite anode Raman spectra during NiO reduction in hydrogen, after subtraction of the ground signal.

The ground lines were fitted selecting 7 nodal points: 700, 800, 900, 1000, 1250, 1500 and 2000 cm^{-1} . These curves were subtracted from the starting spectra. The results (Fig.9) clearly indicate disappearance of the characteristic phonon peak on the reduction of NiO in flowing hydrogen, since metallic Ni exhibits no peaks in this range of the Raman shifts. The time dependence of the peak maximum and area is displayed in Fig.10. Following initial plateau-like behavior, the kinetics can be described by a standard parabolic law typical for diffusion-limited redox processes involving binary metal oxides, such as NiO. The trends, observed when oxygen anions are supplied through the solid electrolyte membrane, and relevant microscopic mechanisms will be analyzed in forthcoming reports.

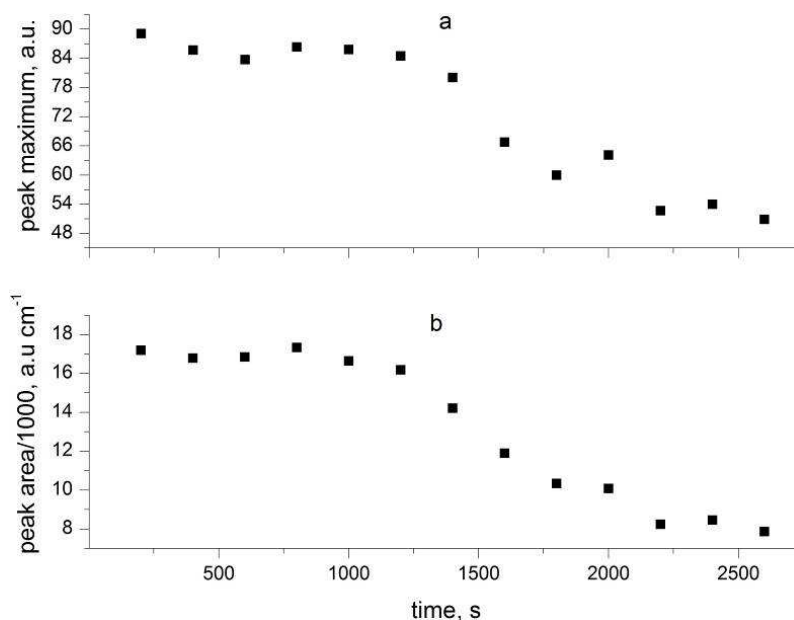


Figure 10. Time dependence of the 2P peak height (a) and area (b) during NiO reduction in the composite anode layer.

Conclusions

A novel combined approach for *in-situ* Raman spectroscopy analysis of local chemical and electrochemical reactions in the vicinity of SOFC electrode | electrolyte interface was proposed. The experimental technique is based on the use of SOFC-type cells comprising optically transparent single-crystal membranes of stabilized cubic zirconia, placed under oxygen chemical potential gradient in the controlled-atmosphere chamber. In combination with the electrochemical measurements, this technique makes it possible to directly study the redox processes induced in the triple-phase boundary zone by variations of the current density, temperature and gaseous phase composition. The experimental setup was tested in the regime of Ni-containing cermet anode reduction.

Acknowledgments

This work was supported by the Russian Foundation for Basic Research (grant 14-29-04031) and the Ministry of Education and Science of the Russian Federation (grant 14.B25.31.0018).

References

1. R. C. Maher, V. Duboviks, G. J. Offer, M. Kishimoto, N. P. Brandon, L. F. Cohen, *Fuel Cells*, **13** (4), 455 (2013)
2. X. Q. Sha, Z. Lu, X. Q. Huang, J. P. Miao, Z. H. Ding, X. S. Xin, W. H. Su, *J Alloy Compd.*, **428** (1-2), 59 (2007)

3. Y. Ji, J. Liu, T. M. He, J. W. Wang, W. H. Su, *J Alloy Compd.*, **389** (1-2), 317 (2005)
4. B. Matovic, Z. Dohcevic-Mitrovic, M. Radovic, Z. Brankovic, G. Brankovic, S. Boskovic, Z. V. Popovic, *J. Power Sources*, **193** (1), 146 (2009)
5. J. Dong, Z. Cheng, S. W. Zha, M. L. Liu, *J. Power Sources*, **156** (2), 461 (2006)
6. J. F. B. Rasmussen, A. Hagen, *J. Power Sources*, **191** (2), 534 (2009)
7. J. N. Kuhn, N. Lakshminarayanan, U. S. Ozkan, *J. Mol. Catal. A Chem.*, **282** (1-2), 9 (2008)
8. W. Zhou, J. Sunarso, Z. G. Chen, L. Ge, J. Motuzas, J. Zou, G. X. Wang, A. Julbe, Z. H. Zhu, *Energ. Environ. Sci.*, **4** (3), 872 (2011)
9. K. T. Lee, A. A. Lidie, S. Y. Jeon, G. T. Hitz, S. J. Song, E. D. Wachsman, *J. Mater. Chem. A*, **1** (20), 6199 (2013)
10. Y. H. Chen, J. Xu, Y. J. Wei, X. Q. Liu, G. Y. Meng, *Chinese J. Inorg. Chem.*, **22** (11), 1941 (2006)
11. P. H. Larsen, F. W. Poulsen, R. W. Berg, *J. Non Cryst. Solids*, **244** (1), 16 (1999)
12. B. Tiwari, A. Dixit, G. P. Kothiyal, *Int. J. Hydrogen Energ.*, **36** (22), 15002 (2011)
13. A. A. Reddy, N. Egtesadi, D. U. Tulyaganov, M. J. Pascual, L. F. Santos, S. Rajesh, F. M. B. Marques, J. M. F. Ferreira, *J. Eur. Ceram. Soc.*, **34** (5), 1449 (2014)
14. N. Orlovskaya, A. Coratolo, C. Johnson, R. Gemmen, *J. Am. Ceram. Soc.*, **87** (10), 1981 (2004)
15. J. Puranen, M. Pihlatie, J. Lagerbom, T. Salminen, J. Laakso, L. Hyvarinen, M. Kylmalahti, O. Himanen, J. Kiviaho, P. Vuoristo, *Int. J. Hydrogen Energ.*, **39** (30), 17246 (2014)
16. T. Y. Yung, H. P. Tseng, P. Yang, L. K. Liu, *Mater. Res. Innov.*, **17**, 129 (2013)
17. M. B. Pomfret, J. C. Owrutsky, R. A. Walker, *Anal. Chem.*, **79** (6), 2367 (2007)
18. Z. Cheng, M. L. Liu, *Solid State Ionics*, **178** (13-14), 925 (2007)
19. M. B. Pomfret, J. Marda, G. S. Jackson, B. W. Eichhorn, A. M. Dean, R. A. Walker, *J. of Physical Chemistry C*, **112** (13), 5232 (2008)
20. B. C. Eigenbrodt, M. B. Pomfret, D. A. Steinhurst, J. C. Owrutsky, R. A. Walker, *J. Phys. Chem. C*, **115** (6), 2896 (2011)
21. J. D. Kirtley, D. M. Halat, M. D. McIntyre, B. C. Eigenbrodt, R. A. Walker, *Anal. Chem.*, **84** (22), 9745 (2012)
22. Y. Kim, J. H. Kim, J. Bae, C. W. Yoon, S. W. Nam, *J. Phys. Chem. C*, **116** (24), 13281 (2012)
23. Kishimoto, K. Yashiro, T. Shimonosono, M. E. Brito, K. Yamaji, T. Horito, H. Yokokawa, J. Mizusaki, *Electrochim. Acta*, **82**, 263 (2012)
24. Schiller, C. Auer, W. G. Bessler, C. Christenn, Z. Ilhan, P. Szabo, H. Ax, B. Kapadia, W. Meier, *J. Appl. Phys. B Lasers O.*, **111** (1), 29 (2013)
25. Nagai, F. Iguchi, S. Onodera, N. Sata, T. Kawada, H. Yugami, *ECS Trans.*, **35** (1), 519 (2011)
26. M. A. Borik, E. E. Lomonova, V. V. Osiko, V. A. Panov, O. E. Porodnikov, M. A. Vishnyakova and Yu. K. Voron'ko, V. V. Voronov, *J. Cryst. Growth*, **275**, e2173 (2005).
27. V. I. Aleksandrov, V. V. Osiko, A. M. Prokhorov and V. M. Tatarintsev, *Russ. Chem. Rev.*, **47** (3), 213 (1978).

28. V. G. Artemov, I. E. Kuritsyna, S. P. Lebedev, G. A. Komandin, P. O. Kapralov, I. E. Spektor, V. V. Kharton, S. I. Bredikhin and A. A. Volkov, *Russ. J. Electrochem.*, **50** (7), 690 (2014)
29. I. S. Bredikhin, F. S. Napol'skii, E. V. Korovkin, S. Y. Istomin, E. V. Antipov, S. I. Bredikhin, *Russ. J. Electrochem.*, **45**, 434 (2009)
30. I. Burmistrov, D. Agarkov, S. Bredikhin, Y. Nepochatov, O. Tiunova, O. Zadorozhnaya, *ECS Trans.*, **57** (1), 917 (2013)